J. Fluid Mech. (2021), *vol*. 911, A22, doi:10.1017/jfm.2020.1074

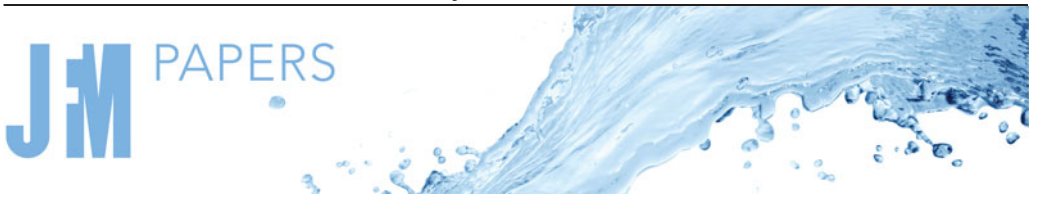

Viscous resuspension of non-Brownian particles: determination of the concentration profiles and particle normal stresses

Enzo d'Ambrosio[1], **Frédéric Blanc**[1] **and Elisabeth Lemaire**[1],†

[1]Université Côte d'Azur, CNRS, InPhyNi-UMR 7010, 06108 Nice CEDEX 2, France

(Received 1 April 2020; revised 16 August 2020; accepted 25 November 2020)

We perform local measurements of both the velocity and the particle volume fraction to study viscous resuspension in non-Brownian suspensions for Shields numbers ranging from 10^{-3} to 1. With this aim, a suspension of polymethacrylate spherical particles dispersed in a lighter Newtonian fluid (Triton X100) is sheared in a vertical Couette cell where both velocity and particle density mappings are performed. We show that the radial profiles of the velocity and of the particle volume fraction are inconsistent in the framework of local rheology of a Newtonian material and that these discrepancies disappear for a neutrally buoyant suspension. The vertical concentration profiles are used to deduce the third particle normal stress, Σ_{33}^p, by solving the Cauchy equation. The value of Σ_{33}^p is shown not to vary linearly with shear rate but rather through a power law with an exponent close to 0.7, irrespective of the value of the particle volume fraction, in accordance with the recent results of Saint-Michel *et al.* (*Phys. Fluids*, vol. 31, 2019, 103301). Finally, we compare our results with the results of previous studies where $\alpha_3 = \Sigma_{33}^p/\eta_0\dot{\gamma}$ (with η_0 the viscosity of the suspending liquid and $\dot{\gamma}$ the shear rate) was deduced from the macroscopic measurement of the height of the resuspended layer. The agreement is satisfactory.

Key words: granular media, suspensions, particle/fluid flow

1. Introduction

Understanding the flow properties of concentrated suspensions is a real challenge in the development of many industrial products (e.g. solid propellant rocket motors and fresh concrete) and in the description of various environmental flows (e.g. torrential lava, mud flows and submarine slides). Among other transport properties, shear-induced particle migration has received increasing attention in recent decades. Particle migration can be due to inertial effects (Segre & Silberberg 1962) but also occurs at low Reynolds numbers,

† Email address for correspondence: elisabeth.lemaire@unice.fr

for instance, in a Poiseuille flow in which the particles tend to migrate towards the centre of the channel (Koh, Hookham & Leal 1994; Hampton *et al.* 1997; Butler & Bonnecaze 1999; Snook, Butler & Guazzelli 2016), in wide-gap Couette flow towards the outer cylinder (Abbott *et al.* 1991; Graham *et al.* 1991; Chow *et al.* 1994; Sarabian *et al.* 2019) and outward in the cone-and-plate geometry (Chow *et al.* 1995).

Another typical example of shear-induced migration is viscous resuspension, whereby an initially settled layer of negatively buoyant particles expands vertically when a shear flow is applied. Viscous resuspension was observed for the first time by Gadala-Maria (1979) and later explained by Leighton & Acrivos (1986) and Acrivos, Mauri & Fan (1993), who demonstrated that the height of the resuspended particle layer results from the balance between a downward gravitational flux and an upward shear-induced diffusion flux. The authors studied the resuspension of various particles (different sizes and densities) in two different liquids (different viscosities and densities) sheared in a cylindrical Couette device. They measured the height of the resuspended layer of particles, h_s, as a function of the shear rate and showed that the difference between h_s and h_0 (i.e. the initial sediment height) normalized by h_0 was a function of only the Shields number defined as the ratio between viscous and buoyancy forces

$$\frac{h_s - h_0}{h_0} = f(A) \quad \text{with } A = \frac{9}{2}\frac{\eta_0 \dot{\gamma}}{\Delta\rho g h_0}, \tag{1.1}$$

where $\dot{\gamma}$ is the shear rate, $\Delta\rho$, the density mismatch and η_0, the viscosity of the suspending fluid. Their experimental results were found to be in very good agreement with the diffusive flux model developed by Leighton & Acrivos (1986). Later, Zarraga, Hill & Leighton (2000) revisited the results of Acrivos *et al.* (1993) to determine the particle normal stress in the vorticity direction, Σ^p_{33}, from the height of the resuspended layer of particles by writing the Cauchy momentum balance in the vertical direction

$$\frac{\partial \Sigma^p_{33}}{\partial z} = \Delta\rho g \phi. \tag{1.2}$$

where g is the acceleration of gravity.

Then, a relation between Σ^p_{33} and the particle volume fraction at the bottom, ϕ_0, is obtained by the integration of (1.2) from the interface between the suspended layer and the clear liquid at the bottom together with the equation of particle number conservation. The relationship between particle normal stress and shear-induced migration (or resuspension) has been the subject of several studies and is still an active area of investigation (Nott & Brady 1994; Mills & Snabre 1995; Morris & Brady 1998; Morris & Boulay 1999; Deboeuf *et al.* 2009; Lhuillier 2009; Nott, Guazzelli & Pouliquen 2011; Ovarlez & Guazzelli 2013). The suspension balance model proposed by Morris & Boulay (1999) and refined by Lhuillier (2009) and Nott *et al.* (2011) offers a promising framework for modelling shear-induced particle migration, but it suffers from a relative lack of experimental data on particle normal stresses.

In addition to the above-cited work of Zarraga *et al.* (2000), who used the viscous resuspension experiment of Acrivos *et al.* (1993) to deduce Σ^p_{33} for particle volume fractions ranging from 0.3 to 0.5, Deboeuf *et al.* (2009) determined Σ^p_{33} for particle volume fractions ranging from 0.3 to 0.5 through the measurement of the pore pressure in a cylindrical Couette flow. Boyer, Guazzelli & Pouliquen (2011) used a pressure-imposed shear cell to measure Σ^p_{22} in the range $\phi \in [0.4, 0.585]$, and Dbouk, Lobry & Lemaire (2013) determined Σ^p_{22} in the range $\phi \in [0.3, 0.47]$ through the measurement of both the total stress Σ_{22} and the pore pressure. See Guazzelli & Pouliquen (2018) for a review.

All of these studies show a quasi-linear relationship between the particle normal stress components and the shear rate, but recently, Saint-Michel *et al.* (2019) performed X-ray radiography experiments on viscous resuspension that revealed a nonlinear relationship with the shear rate.

In this paper, we present the experimental results of viscous resuspension in a Couette device in which the local particle volume fraction and the local shear rate are measured by optical imaging. The value of Σ^p_{33} is obtained by integrating (1.2) from the interface between the clear fluid and the resuspended layer to any height z below the interface. These experiments present the dual advantage that Σ^p_{33} can be determined for a wide range of particle fractions and that the local shear rate can be measured to accurately test the scaling of particle normal stresses with shear rate. In § 2, we present the experimental device and the methods used to compute both the velocity field and the particle concentration field, for Shields numbers ranging from 10^{-3} to 1. Section 3 is devoted to the results. We first discuss the radial profiles of velocity and of particle concentration. Then we present the vertical concentration profiles from which Σ^p_{33} is deduced. We finish with some concluding remarks (§ 4).

2. Materials and methods

2.1. *Suspension and device*

Polymethacrylate (PMMA) spheres (Arkema BS572), $2a = 268 \pm 25$ μm in diameter and $1.19 \times 10^3 \pm 10$ kg m^{-3} in density, are used. The particles are dispersed in Triton X 100 to which a small amount of a fluorescent dye (Nile Blue A, Sigma-Aldrich) is added. This mixture is Newtonian with a viscosity of $\eta_0 = 0.34 \pm 0.02$ Pa s and a density $1.06 \times 10^3 \pm 10$ kg m^{-3} at $T = 23\,^\circ$C. The characteristic settling velocity of the particles is then $V_S = 2/9\Delta\rho g/a^2\eta \approx 20$ μm s^{-1}. The liquid and the particles are chosen to have roughly the same refractive index, 1.49, and accurate index matching is achieved by tuning the temperature of the chamber that contains the rheometer.

The resuspension experiments are conducted in a Couette cell made of PMMA mounted on a controlled-stress rheometer (Mars II, Thermofisher) (see figure 1*a*). The rotor has a radius $R_1 = 19$ mm, and the stator has a radius $R_2 = 24$ mm. Thus, the gap is much larger than the particle diameter ($(R_2 - R_1)/a \approx 37$) and the variation of the shear stress over the gap is expected to be of the order of 1.6 ($\Sigma_{12}(R_1)/\Sigma_{12}(R_2) = R_2^2/R_1^2 \approx 1.6$). The impact of the stress variation on particle migration will be discussed in § 3.1.

The bottom of the Couette cell is filled with mercury to prevent the particles from migrating out of the gap (under the cup) and to maximize slip at the suspension/bottom interface in order to have a shear rate as homogeneous as possible inside the gap. The suspension is poured into the rheometer cell and illuminated by a thin vertical laser sheet (thickness ≈50 μm) offset by $y_0 = 16.2$ mm from the radial plane (see figure 1*b*). A camera (IDS, nominal frequency 33 Hz, full resolution 4104×2174 px^2) is placed at 90° to the enlightened plane. The accurate matching of the refractive index, the thinness of the laser sheet and the resolution of the camera allow the recording of high-quality images with a resolution of 30 px per particle.

2.2. *Experimental procedure and measurement method*

2.2.1. *Experimental procedure*

In this paper, we will focus on the steady state of resuspension obtained for various angular velocities of the rotor, Ω: 0.3, 0.5, 1, 2, 5, 10, 20, 30, 40 and 60 rotations per minute (r.p.m.). For all these angular velocity values, the Reynolds number and the Taylor number are less than 1 (for the highest angular velocity, $\mathcal{R}e = \rho\Omega R_1(R_2 -$

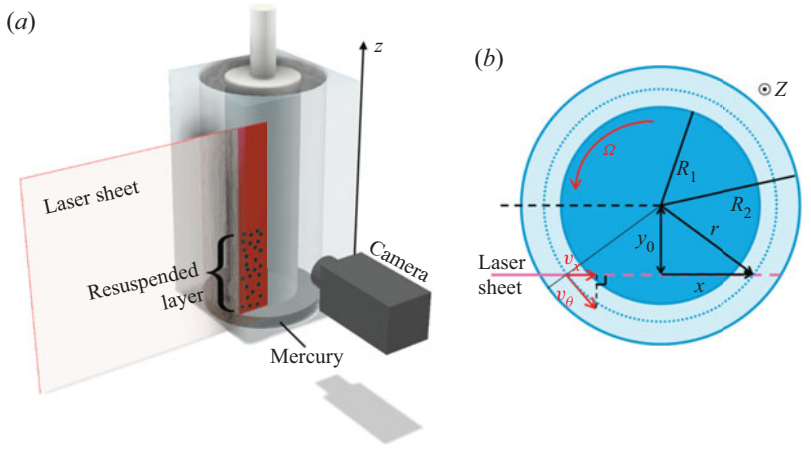

Figure 1. (*a*) Sketch of the experimental device. (*b*) View from above. The vertical laser sheet is shifted by an offset of length $y_0 < R_1$ from the radial position (dashed line); x is the horizontal position in the laser sheet, and z is the vertical position; $z = 0$ is set by the mercury/suspension interface.

$R_1)/\eta \approx 1$ and $Ta = 4\rho^2\Omega^2(R_2 - R_1)^4/\eta^2 \approx 1$) and the Péclet number is very large ($\mathcal{P}e = 6\pi\eta a^3\dot{\gamma}/k_BT > 10^8$, with k_B the Boltzmann constant). Note that the inertial effects have also to be compared with the gravity forces. The ratio of inertial to gravitational forces can be written as $R_i\Omega^2/g$. In our experiment this number is comprised between 10^{-6} and 10^{-1}, meaning that inertial effects can indeed be neglected. Furthermore, beyond this simple evaluation, Saint-Michel *et al.* (2019) performed two-dimensional calculations to evaluate the role of the centrifugal forces that arise due to geometry curvature and showed that inertia effects do not alter the concentration profiles for $R_i\Omega^2/g < 1$.

To reach the steady state, the suspension is first sheared with an angular velocity of the rotor equal to 5 r.p.m. for one hour. Then, the speed is set to the desired value for a period until the steady state is reached; the steady state is considered attained when the torque applied by the rheometer becomes constant. The time duration necessary to achieve the steady state is approximately a few hours. Figure 2 shows the viscous resuspension observed for a few rotor angular velocity values. As Ω increases, the resuspended height increases and the bulk particle concentration decreases.

2.2.2. *Settled layer*

The first (left upper) image of figure 2 shows an image of the suspension in the settled state. The sediment height is $h_0 = 21.3$ mm $\approx 4(R_2 - R_1)$. It is really important to determine as precisely as possible the value of the packing fraction in the sediment, ϕ_0, since it will subsequently be used to deduce the particle volume fraction during the resuspension experiments (see § 2.2.3). Here, ϕ_0 is the ratio of volume of the particles that belong to the sediment to the total volume of the sediment. Thus, to evaluate ϕ_0, it is necessary to know the exact quantity of particles in the sediment and to measure the total volume of the sediment. Unfortunately, it is difficult to accurately control the mass of particles that are poured into the Couette cell. Thus, we decided to measure ϕ_0 in a separate vessel. With this aim, a known mass of particles, m_p, is introduced in a graduated cylinder of known cross-section (approximately 1 cm^2), S, that contains the suspending liquid (Triton X100). After the particles have settled (approximately after 24 h), the sediment height, h_{sed} is carefully measured and ϕ_0 is deduced ($\phi_0 = m_p/(\rho_p h_{sed} S)$). We took three measurements and obtained $\phi_0 = 0.574 \pm 0.003$.

2.2.3. *Concentration field determination*

The concentration field is determined through the measurement of the particle number density, n_{ij} in the (x, z) vertical laser plane. With this aim, each image is binarized with a local threshold whose value $T(x, z)$ is calculated individually for each pixel (x, z) of the image $I(x, z)$ where $T(x, z)$ is a weighted sum (cross-correlation with a Gaussian window) of 171×171 px^2 neighbourhood of the pixel (x, z) (see OpenCV adaptiveThreshold https://docs.opencv.org/2.4/index.html). The particles are detected through a watershed segmentation process (Vincent & Soille 1991). The position of the barycentre of each segmented zone gives the position of each particle centre in the (x, z) plane sampled with rectangular cells (i, j) of size $\delta x = (R_2 - R_1)/8$ and $\delta z = 2a$. In each cell, the number of particle centres, N_{ij}, is measured. The particle density $n_{ij} = N_{ij}/(\delta x \delta z)$ is reconstructed in the (r, z) plane, making the change of variable $r = \sqrt{y_0^2 + x^2}$. Due to the non-zero thickness of the laser sheet and of the slight polydispersity of the particles, n_{ij} is not the absolute particle density, and to compute the true particle volume fraction, we use the particle volume conservation from the sediment to the resuspended state

$$\phi(r, z) = \chi n(r, z) \quad \text{with } \chi = \frac{\phi_0 \pi (R_2^2 - R_1^2) h_0}{\displaystyle\int_0^{h_s} \int_{R_1}^{R_2} n_{ij} 2\pi r \, \mathrm{d}r \, \mathrm{d}z}. \tag{2.1}$$

Note that the determination of $\phi(r, z)$ from the measurement of $n(r, z)$ is not the method that is most widely used. The more standard approach consists of measuring the area of particles intersected by the laser sheet (see for instance Sarabian *et al.* (2019) or Snook *et al.* (2016)). In appendix A, we justify the choice of the method that has been used. With this aim, the vertical concentration profile in a neutrally buoyant suspension is determined from the two methods. We show that considering the particle area crossed by the laser sheet introduces a bias that is less pronounced when the particle concentration is determined from the particle number density.

The mean particle volume fraction is computed by repeating the image analysis over 10 000 decorrelated images (with the exception of the sediment for which only 20 images were used). The acquisition time can be as long as 100 h for the lowest rotation speed of the rotor. Examples of the concentration field are given in figure 2, which raises some comments that will be discussed in more detail in § 3:

(i) Near the walls, the particle fraction is lower than in the bulk of the suspension, which should stem from the layering of the particles near the walls (Suzuki *et al.* 2008; Yeo & Maxey 2010; Blanc *et al.* 2013; Gallier *et al.* 2016; Deboeuf *et al.* 2018).

(ii) Outside of the structured zones, no or very weak radial particle migration is observed: the maximum difference in the particle volume fraction is evaluated to be less than 2 %.

(iii) Along the vertical direction, a negative concentration gradient is observed as expected in the case of resuspension flows with a sharp interface separating the suspension and the pure fluid (Acrivos, Fan & Mauri 1994).

(iv) Near the bottom on the rotor side, the particle volume fraction decreases by approximately 2 %. This will be discussed in more detail in § 3.2 and in appendix A but from this observation we can evaluate the resulting uncertainty on χ and thus on the absolute value of $\phi(r, z)$. The area affected by the concentration change is approximately one tenth of the sediment leading an uncertainty of 0.3 % on the particle volume fraction.

2.2.4. *Velocity fields*

The aim of the present study is to investigate resuspension and to link it to particle normal stresses. Because Σ_{33}^{p} is a function of the shear rate, it is essential that the shear rate is known as precisely as possible. For this purpose, we measured the velocity field in the gap. The shift in the laser sheet out of the radial plane allows particle image velocimetry (PIV) measurements (Manneville, Bécu & Colin 2004) in the (x, z) plane. Under the assumption that the radial component of the velocity is zero or much smaller than the azimuthal component, v_θ can be deduced from a simple projection of v_x along the orthoradial direction (see figure 1*b*)

$$v_\theta(x, z) = v_x(x, z)\frac{\sqrt{x^2 + y_0^2}}{y_0}. \tag{2.2}$$

The velocity field $\boldsymbol{v}(v_x(x, z), v_z(x, z))$ is computed using the open source software DPIVSOFT (available on the web (https://www.irphe.fr/meunier/)) (Meunier & Leweke 2003). Each image is divided into correlation windows of size 128×128 px^2. Each correlation window contains approximately 10 particles that are the PIV tracers. The cross-correlation of the corresponding windows from two successive images yields the mean velocity of the particles in the window. The in-plane loss of pairs error is decreased by translating the correlation windows in a second run (Westerweel 1997), thus reducing the correlation windows size to 64×64 px^2. The same procedure performed on all the windows gives the velocity field, which is averaged over 100 images.

The mapping of the θ-component of the velocity field in the plane (x, z) is then obtained and used to reconstruct the velocity field in the (r, z) plane. Velocity maps are shown in figure 2, in which the velocity normalized by the velocity of the rotor is represented for several values of Ω.

Note that the PIV measurements also enable estimation of the z-component of the velocity, particularly to check that there is no significant secondary flow. The second normal stress difference is known to be responsible for secondary flows arising in non-axisymmetric conduits, resulting in non-trivial concentration distributions (Ramachandran & Leighton 2008). Some evidence of secondary flows in cylindrical Couette flow has been given by Blaj *et al.* (2011) who show examples of three-dimensional trajectories of a tracer introduced in a concentrated non-Brownian suspension. It is difficult to deduce any general features of secondary flow from these trajectories, which furthermore are likely to depend on the disturbances created at the bottom. Then, in order to attempt to characterize any potential secondary flow, the axial velocity, v_z is registered and mapped, as showed in figure 2(*d*). As expected, the axial component of velocity is very small compared with the azimuthal component and, more interestingly, no peculiar spatial correlation is detected, perhaps with the exception of a slight tendency of an upward motion of the particles near the rotor and a downward motion near the stator.

3. Results

3.1. *Radial profiles*

3.1.1. *Concentration profiles*

First, we estimate the radial distribution of particles inside the sediment. The concentration measurement is based on only 20 images. We have not been able to take more images since it takes approximately one day for the concentration to become steady in the sediment. Thus the statistical error is expected to be as large as 5 % and only an estimate of $\phi(r)$ can be obtained in the sediment. Figure 3(*a*) shows this estimation for three heights: $z =$

$h_0/4$, $h_0/2$, $3h_0/4$, where ϕ has been averaged over a height of $\pm 0.15h_0$. Apart from near the rotor and stator where indistinct particle layering is observed, the particle volume fraction is constant along the gap. This expected result indicates in particular that the image processing used to detect particles is reliable. The measurement of the radial concentration profiles is rather important since, in cylindrical Couette flow, outward radial migration is expected in concentrated non-Brownian suspensions (Abbott *et al.* 1991; Graham *et al.* 1991; Phillips *et al.* 1992; Chow *et al.* 1995; Sarabian *et al.* 2019). Figures 3(*b*) and 3(*c*) show concentration profiles measured at 3 heights: $z = h_s/4$, $h_s/2$, $3h_s/4$, and z-averaged over one tenth of the resuspended layer and over 10 000 frames for two selected angular velocities: $\Omega = 0.3$ (*b*) and 20 r.p.m. (*c*). For both angular velocities, a particle layering is observed and is all the more pronounced when the angular velocity is low (or the particle volume fraction is high). Particle layering in concentrated non-Brownian suspensions is well documented and has been specifically addressed by numerical simulations (Yeo & Maxey 2010; Gallier *et al.* 2016) and observed in many experiments (Blanc *et al.* 2013; Metzger, Rahli & Yin 2013; Deboeuf *et al.* 2018; Sarabian *et al.* 2019). Note that, in the structured zones, the absolute value of ϕ is not relevant since the spatial resolution $\delta x = (R_2 - R_1)/200 \approx 2a/10$ is much smaller than the characteristic distance between particle centres ($O(2a)$). Thus, since the radial position of the particles is fixed in the layered zone, the determination of the particle number density depends on the sample size. A high spatial resolution has been chosen in order to evidence the layering but the counterpart is that the values of ϕ in the structured zones are not proper, only their variation is significant. Outside the layered zones, where particles are randomly distributed, we have checked that the values of ϕ do not vary with sampling size (this is also observable in figure 13).

Outside the structured zones near the rotor and the stator, the concentration profiles are observed to be z-dependent but, at a given height, they are almost flat (see insets of figure 3*b*,*c*). This trend is verified for all angular velocities, including those that are not shown in the present paper (see supplementary material available at https://doi.org/10.1017/jfm.2020.1074 for more information).

This finding contrasts with the predictions of the suspension balance model (SBM) (Morris & Boulay 1999) that are also shown in figures 3(*b*) and 3(*c*) (dashed lines). In the framework of a one-dimensional flow (this assumption will be discussed in the next section and in more detail in the supplementary material), according to the SBM, concentration profiles obey the following equation:

$$q(\phi) = \frac{\eta_N}{\eta_S} = Ar^{(1+\lambda_2)/\lambda_2}, \tag{3.1}$$

where $\eta_N = \Sigma_{11}^p/\eta_0\dot{\gamma}$ is the normal viscosity, η_S the relative viscosity and λ_2 a constant close to 1 (here, we took $\lambda_2 = 1/1.15$). The value of A is a constant determined by requiring particle volume conservation. The theoretical profiles of figures 3(*b*) and 3(*c*) are obtained with the expressions of η_N and η_S proposed by Zarraga *et al.* (2000)

$$\left.\begin{aligned} \eta_S &= \frac{\exp(-2.34\phi)}{\left(1 - \dfrac{\phi}{\phi_m}\right)^3}, \\ \eta_N &= 2.17\phi^3\eta_S \exp(2.34\phi). \end{aligned}\right\} \tag{3.2}$$

Such discrepancies between SBM predictions and experiments conducted in cylindrical Couette flow have already been reported by several authors (see for instance Ovarlez, Bertrand & Rodts (2006); Colbourne *et al.* (2018) and Gholami *et al.* (2018) and to a

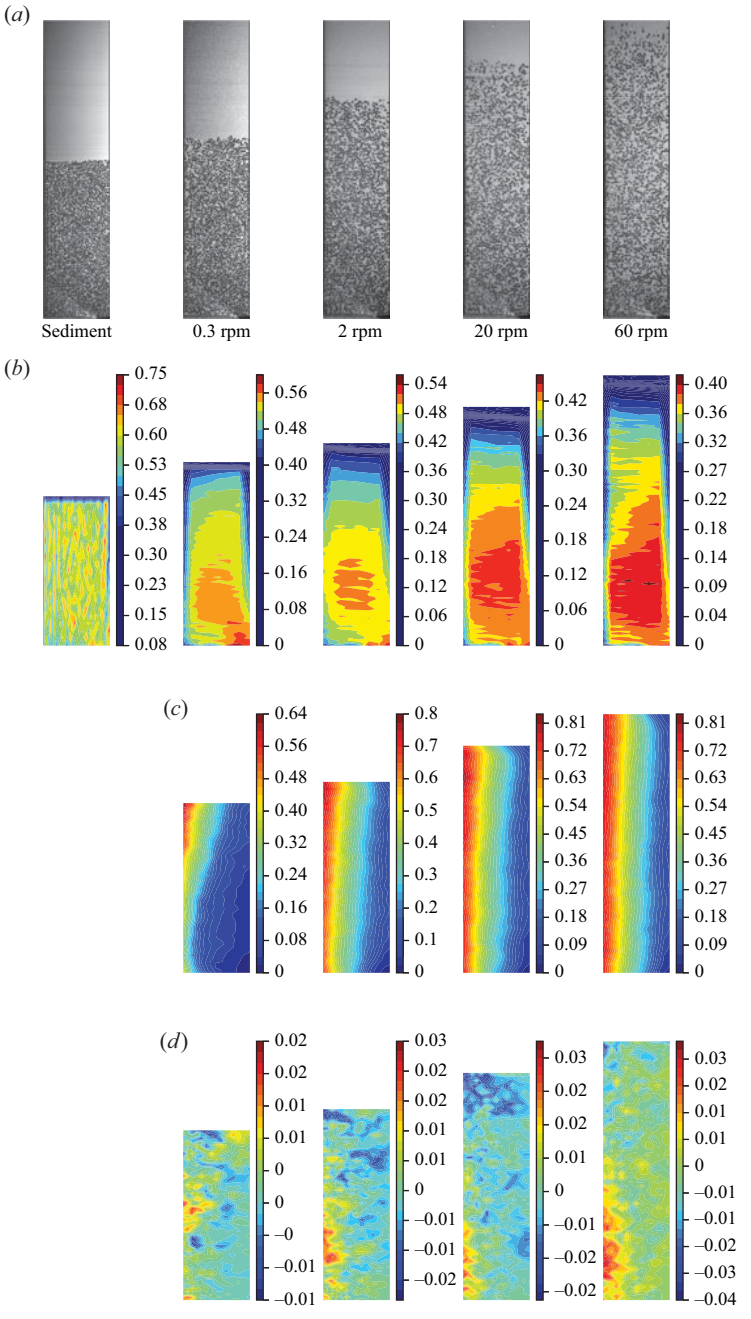

Figure 2. (*a*) Typical images recorded for different rotor rotation speeds. A photo of the settled layer ($\Omega = 0$) is also presented (height 21.3 mm). (*b*) Mapping of the particle volume fraction averaged over 10 000 images (with the exception of the sediment for which only 20 images have been used). (*c*) Azimuthal velocity normalized by the rotor velocity ΩR_1 and averaged over 100 velocity fields. (*d*) Vertical velocity normalized by ΩR_1 and averaged over 100 velocity fields. The rotor is on the left of each frame, the stator is on the right and the mercury/suspension interface corresponds to the bottom of each frame.

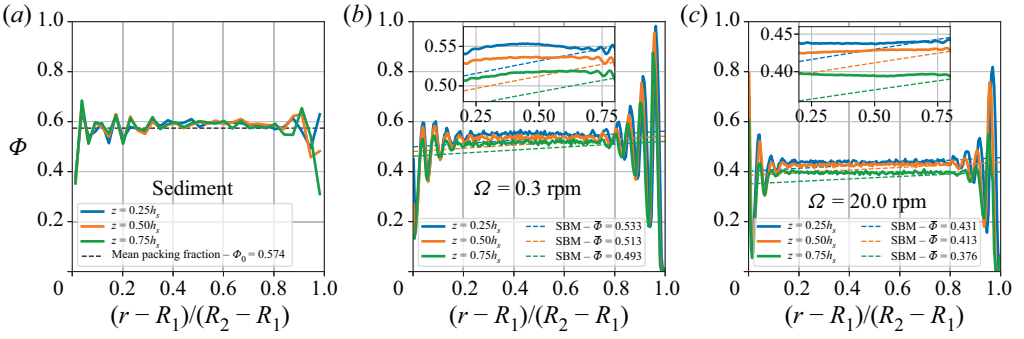

Figure 3. Radial concentration profiles in the sediment (*a*) and in the resuspended layer for two values of the rotation speed (*b*,*c*) and three heights. The radial profile in the sediment is computed from 20 images with a radial sampling $\delta x = (R_2 - R_1)/30$ and a z-averaging of $\pm 0.15 h_0$. The radial profiles of (*b*,*c*) are computed from 10 000 images with a radial sampling $\delta x = (R_2 - R_1)/200$ and a z-averaging of $\pm 0.05 h_s$. Particle layering near the rotor and the stator is observed. Outside these zones (see insets) the measured profiles (solid lines) are almost flat in contrast to the predictions of the suspension balance model (Morris & Boulay 1999) computed for $\bar{\Phi}$ that is the r-averaged volume fraction at a given z (dashed lines).

lesser extent Sarabian *et al.* (2019)). The layering of the particles near the walls probably plays a role, but is not likely to account for the entire discrepancy. As suggested in Gholami *et al.* (2018), top and bottom boundary effects may also invalidate the use of the SBM in its one-dimensional formulation. Another hypothesis would be that radial size segregation is involved since the particles are not perfectly monodisperse (with a standard deviation of approximately 8 %, see supplementary material for more detail). The larger particles are expected to migrate faster than the smaller ones and then to be focused on the outside. This size segregation effect has been noted by Abbott *et al.* (1991) in a bimodal suspension containing 3175 and 780 μm particles with respective volume fractions of 0.39 and 0.21 sheared in a wide-gap Couette rheometer ($R_1 = 6.4$ mm and $R_2 = 23.8$ mm). After a few thousand revolutions of the inner cylinder, the larger particles are observed to form hexagonally close-packed sheets near the stator. In our study, even though the particle size distribution (see supplementary materials) has nothing in common with the bimodal distribution used by Abbott *et al.* (1991), a size gradient across the gap might affect the concentration profiles since, as depicted in § 2.2.3, the particle volume fraction is deduced from the particle number density. More precisely, if the larger particles are preferentially located near the stator, while the region near the rotor is mainly occupied by the smaller ones, the particle volume fraction can increase from the rotor to the stator, even though the particle number density is measured constant across the gap, which would explain why the concentration profiles do not obey SBM predictions. In the supplementary material, we show that there is no evidence in support of the hypothesis. Another explanation would be that migration is modified if there exists an interplay between the resuspension flux associated with density mismatch and the radial migration. Blaj (2012) measured the radial concentration profiles in suspensions of either density-matched or buoyant non-Brownian suspensions sheared in a Couette rheometer and noticed significant differences between the two cases.

In order to discriminate between these two hypotheses (radial size segregation or buoyancy effects), we measured the radial concentration profile in a neutrally buoyant suspension made of the same particles dispersed in a mixture of water, Triton X100 and zinc chloride (density 1.19 g cm^{-3}, viscosity 4.43 Pa s). The results, described in appendix B, show that, contrary to the case of a buoyant suspension, particle migration

clearly takes place. Furthermore, the agreement with the SBM predictions is fairly satisfactory (see figure 13). Note that, to allow a more quantitative comparison between our experimental results and the SBM predictions, we also present the variation of the viscosity of the neutrally buoyant suspension with particle volume fraction and shear stress in appendix C. Thus, since SBM appears to very accurately predict the concentration in the neutrally buoyant suspension, the very weak migration observed in figure 3 for non-neutrally buoyant suspensions is likely to come from the density mismatch between the particles and the fluid that probably leads to an interplay between the vertical and the radial particle fluxes.

3.1.2. *Velocity profiles*

Figure 4 shows the radial velocity profiles that correspond to the concentration profiles of figure 3 ($v(r)$-profiles z-averaged over one tenth of the resuspended layer height for $\Omega = 0.3$ and 20 r.p.m.). The velocity profiles clearly demonstrate a non-Newtonian behaviour of the suspension as well as wall slip, especially in the case of the lower angular velocity, i.e. for the larger particle volume fractions. The wall slip phenomenon in concentrated non-Brownian suspensions is well known (Jana, Kapoor & Acrivos 1995; Ahuja & Singh 2009; Blanc, Peters & Lemaire 2011; Korhonen *et al.* 2015) and is probably related to particle layering near the walls.

In figure 4 we also plot some theoretical velocity profiles. The solid lines correspond to Newtonian profiles, the dashed line to Newtonian profiles with wall slip, the dotted lines to profiles computed from the predictions of the SBM (3.1) and the constitutive law of Zarraga (3.2) with $\phi_m = 0.58$ and the dash-dotted lines are the profiles obtained from (3.1), (3.2) and slip boundary conditions. We used the slip boundary conditions proposed by Jana *et al.* (1995) where the apparent slip velocities at the inner and outer cylinders are given by

$$u_s(R_{1,2}) = \beta_{1,2} a \dot{\gamma}_{1,2} \quad \text{with } \beta_{1,2} = \beta(\phi_{1,2}) \approx \frac{\eta_S(\phi_{1,2})}{8}, \tag{3.3}$$

where $\phi_{1,2}$ and $\dot{\gamma}_{1,2}$ are respectively the particle volume fraction and the shear rate at the rotor and at the stator.

For $\Omega = 20$ r.p.m., the combination of wall slip and SBM allows for a rough description of the experimental profiles. But we have to keep in mind that the particle volume fraction profiles predicted by the SBM appreciably differ from the experimental profiles. Recent work of Colbourne *et al.* (2018) shows the same trend with velocity profiles compatible with the SBM predictions while the particle volume fraction profiles are much flatter than expected from the SBM. For $\Omega = 0.3$ r.p.m., none of the tested models (Newtonian, Newtonian + wall slip, SBM or SBM + wall slip) fits the experimental profiles and the shear seems to localize near the rotor, even for particle fractions lower than the expected jamming fraction (approximately 0.58). Such localization has already been observed by many authors (Huang *et al.* 2005; Ovarlez *et al.* 2006; Blaj 2012) and is generally attributed to the existence of a critical shear rate below which no steady flow exists (Ovarlez *et al.* 2006). Finally, it should be noted that the shear-thinning behaviour that is observed in most concentrated non-Brownian suspensions (Dai *et al.* 2013; Vázquez-Quesada, Tanner & Ellero 2016; Vázquez-Quesada *et al.* 2017; Tanner *et al.* 2018; Lobry *et al.* 2019) cannot alone explain the shape of the profiles. In our experiment, the shear stress varies by a 1.6 factor only, leading to a variation of the viscosity that is far too small to explain the highly non-Newtonian velocity profiles, even for large particle volume fractions (see supplementary materials for a comparison with experimental results).

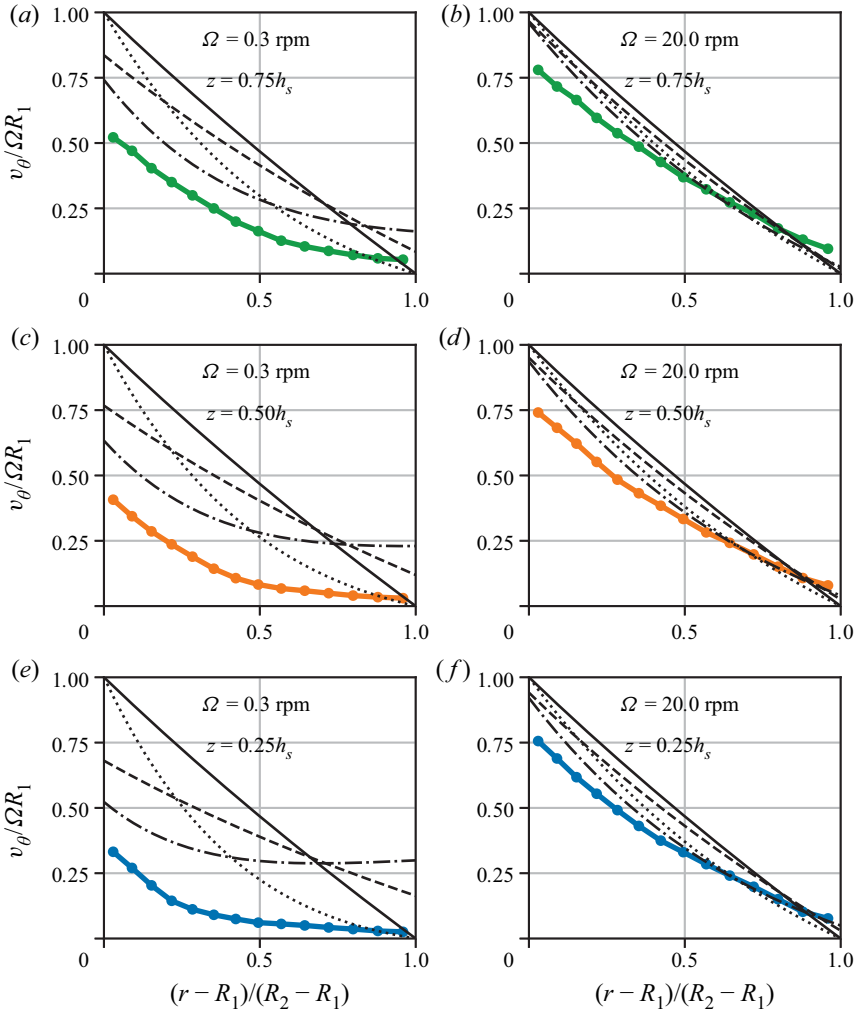

Figure 4. Azimuthal velocity profiles measured for angular velocities: $\Omega = 0.3$ r.p.m. and 20 r.p.m. at three different heights: $h_s/4$, $h_s/2$ and $3h_s/4$. Also shown are the theoretical profiles corresponding to the mean particle volume fraction measured at the corresponding heights. Solid lines: Newtonian profiles without wall slip, dashed lines: Newtonian profiles with wall slip evaluated from Jana *et al.* (1995) (3.3), dotted lines: profiles calculated according to (3.1) and (3.2) without wall slip, dash-dotted lines: profiles calculated according to (3.1) and (3.2) with wall slip (3.3).

We also measured the velocity profile for the neutrally buoyant suspension at $\phi = 0.52$ (see figure 14 in appendix B) and we obtained experimental velocity profiles that are in good agreement with the velocity profiles computed from the predictions of the SBM (3.1) and the constitutive law of Zarraga (3.2) with slip boundary conditions (3.3). As is the case for concentration profiles, the density mismatch between particles and suspending liquid appears to significantly affect the velocity profiles.

3.1.3. *Summary on radial profiles*

(i) Particle layering is observed and the size of the layered zones increases with the volume fraction and is of the order of $8a \approx (R_2 - R_1)/5$ for $\phi \approx 0.55$.

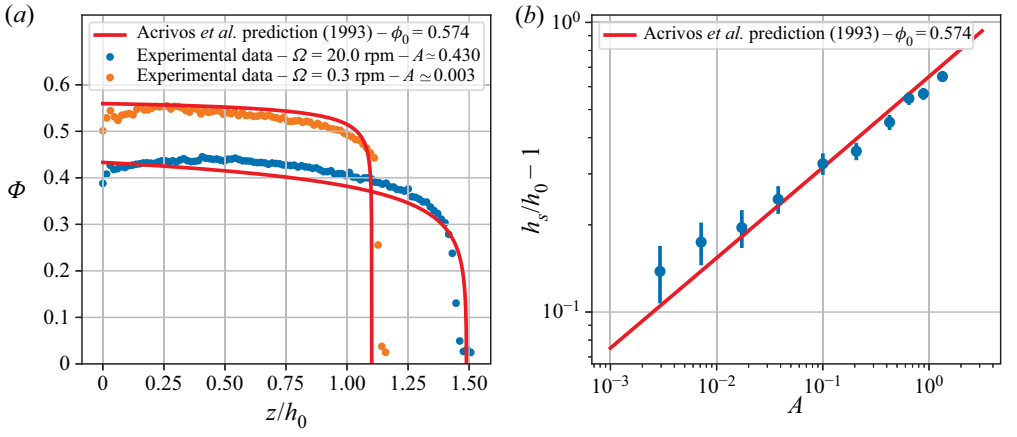

Figure 5. (*a*) Examples of the vertical concentration profiles obtained by averaging $\phi(r)$ over the central third of the gap. The corresponding Shields numbers are computed using the local shear rate (averaged over the central third), and the results are compared with the predictions of Acrivos *et al.* (1993) (red lines). (*b*) Relative expansion of the particle layer versus the Shields number. Here, h_s is arbitrary defined as the height in which $\phi = 0.1$, and the results are compared with the correlation proposed by Acrivos *et al.* (1993).

(ii) Outside these zones, the particle number density hardly varies along r at given z (in contrast with what is observed for a neutrally buoyant suspension, as shown in appendix B).

(iii) The examination of the velocity profiles shows highly non-Newtonian flow characteristics which are not consistent with the measured concentration profiles in the framework of a local Newtonian (or quasi-Newtonian) rheology. Again, the discrepancy between the velocity profiles that are measured or computed from the SBM vanishes for a neutrally buoyant suspension.

3.2. *Vertical concentration profiles*

To study the vertical variation of concentration, we restrict ourselves to the gap region outside the layered zones (where furthermore possible secondary flows may be present) and we focus on the central third of the gap. Figure 5(*a*) shows two concentration profiles averaged over the central third of the gap at low ($\Omega = 0.3$ r.p.m.) and high ($\Omega = 20$ r.p.m.) angular velocities. It is observed that the concentration is almost constant in the resuspended layer and drops to zero quite sharply, even for the highest angular velocity. This sharp interface between the resuspended layer and the clear fluid was already predicted by Acrivos *et al.* (1993) when interpreting their experiments in light of a diffusive flux model. Figure 5(*a*) also shows the profiles predicted by Acrivos *et al.* (1993). The agreement is quite good even though the resuspension height that we measured at low angular velocity is slightly larger than that obtained by Acrivos *et al.* (1993) and marginally smaller at high angular velocity. This trend is seen in figure 5(*b*), where the sediment expansion is plotted against the Shields number. The error bars have been calculated assuming an error of $\pm 2a$ in the determination of both h_S and h_0. In this figure, we observe a power-law dependence of the sediment expansion with the Shields number (1.1), as in Acrivos *et al.* (1993) and Zarraga *et al.* (2000), but with an exponent slightly lower than $1/3$.

Finally, it should be noted that near the bottom of the Couette cell, the particle concentration tends to decrease. This finding may be related either to a problem of particle

detection near the interface with mercury, which reflects light and may downgrade the image quality in its vicinity or to bottom boundary effects which locally modify the flow and particle concentration. In the next section, in which the concentration will be used to evaluate Σ_{33}^p, we will not consider this zone.

3.3. *Determination of* $\alpha_3 = \Sigma_{33}^p/\eta_0\dot{\gamma}$

To estimate $\alpha_3 = \Sigma_{33}^p/\eta_0\dot{\gamma}$, we utilize the region outside the layered zone and well above the suspension/mercury interface: $R_1 + (R_2 - R_1)/3 < r < R_2 - (R_2 - R_1)/3$; $z > h_s/4$.

3.3.1. *Local shear rate*

As shown in § 3.1.2, the velocity profiles are far from what is expected. Thus, to estimate $\alpha_3 = \Sigma_{33}^p/\eta_0\dot{\gamma}$, it is necessary to measure the local shear rate (at least in a wide gap) since it may differ significantly from the macroscopic expected shear rate, called hereafter the nominal shear rate

$$\dot{\gamma}_N(r) = 2\Omega \frac{R_1^2 R_2^2}{R_2^2 - R_1^2} \frac{1}{r^2}. \tag{3.4}$$

Under the assumption that the main component of the shear rate is $\dot{\gamma}_{r\theta}$ and that all the other components are much smaller, the true local shear rate can be deduced from the PIV measurements

$$\dot{\gamma}(r, z) \approx \dot{\gamma}_{r\theta} = r\frac{\partial(v_\theta(r, z)/r)}{\partial r}. \tag{3.5}$$

However, (3.5) presumes that the flow is essentially one-dimensional while two-dimensional characteristics are clearly observed in figure 2, especially for the lowest angular velocity. We have shown that v_z was much smaller than v_θ which makes it valid to neglect the terms that depend on the spatial variation of v_z, but the variation of v_θ with z may not be completely negligible and the component $\partial v_\theta/\partial z$ has to be evaluated before it can be neglected. In the supplementary material, we show that, in most cases, $\partial v_\theta/\partial z \ll r\partial(v_\theta/r)/\partial r$ and that for the lowest angular velocity values and highest particle concentrations, using (3.5) rather than the invariant shear rate introduces an error of, at most, 10 %.

Figure 6 shows the ratio of the measured shear rate (and deduced from (3.5)) to the nominal shear rate deduced from (3.4). It is observed that, for the lowest angular velocities (i.e. the largest ϕ), the shear rate is much lower than expected from (3.4) (except near the rotor). To quantify the difference between $\dot{\gamma}$ and $\dot{\gamma}_N$, we plot the ratio of the measured shear rate averaged over the central third of the gap to the nominal shear rate, $\dot{\gamma}_N$, calculated at the middle of the gap as a function of ϕ for all the values of Ω (figure 7). A few comments on this figure are needed. First, it is observed that all the data collapse onto a unique curve regardless of the angular velocity of the rotor. Second, for low particle volume fractions, $\dot{\gamma}$ tends to $\dot{\gamma}_N$ and $\dot{\gamma} \approx \dot{\gamma}_N$ for $\phi \approx 0.2$. In contrast, for higher concentrations, the local shear rate can substantially deviate from $\dot{\gamma}_N$; for the smallest values of Ω (the largest values of ϕ), the true shear rate can be as small as one fifth of the apparent macroscopic shear rate, making it necessary to measure the velocity field in the gap.

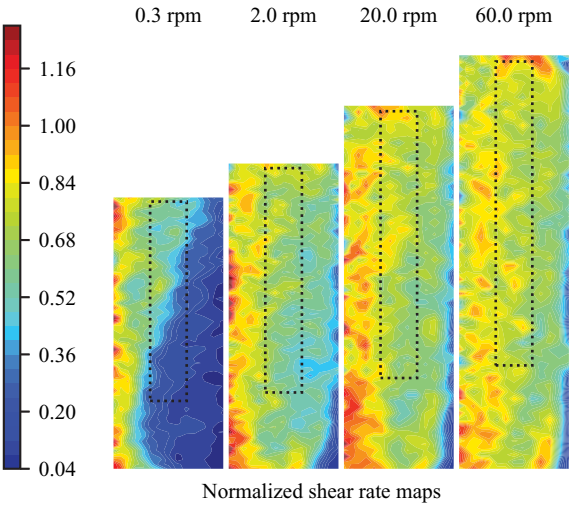

Figure 6. Maps of the measured shear rate $\dot{\gamma}(r, z)$ divided by the expected shear rate $\dot{\gamma}(r)$ for a Newtonian fluid (3.4) for several angular velocities. It is observed that, except near the rotor, the measured shear rate is lower than expected for a Newtonian fluid. The dashed rectangles indicate the areas that are used to measure Σ_{33}^p (figure 9) and to determine the variation of $\Sigma_{33}^p/\eta_0\dot{\gamma}$ with ϕ (figure 10).

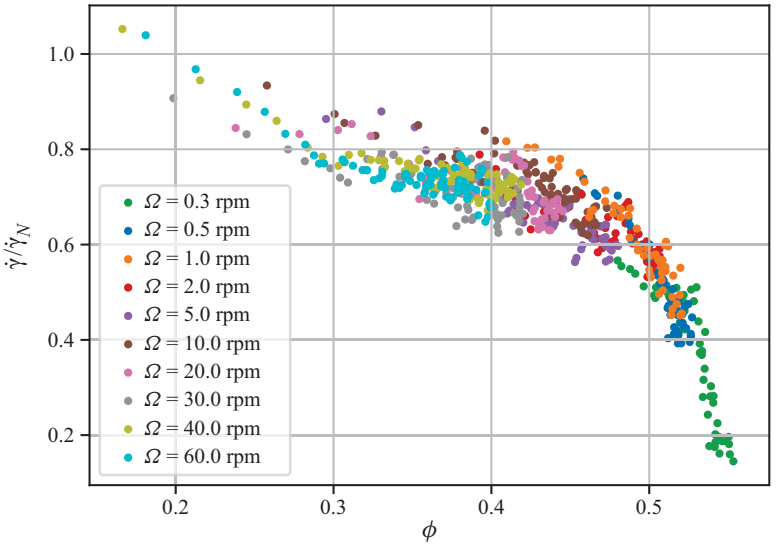

Figure 7. Ratio of the local shear rate to the nominal shear rate vs. the local volume fraction. Each colour corresponds to a given value of Ω. Each point was obtained by averaging $\dot{\gamma}(r, z)$ and $\phi(r, z)$ over the central third of the gap for a given height $z \in [h_s/4, h_s]$. Here, $\dot{\gamma}_N$ is the nominal shear rate calculated at the middle of the gap $r = (R_1 + R_2)/2$.

3.3.2. *Third particle normal stress, Σ_{33}^p*

To determine Σ_{33}^p, (1.2) is integrated from the interface between the resuspended layer and the clear fluid to the height $z(\phi)$

$$\Sigma_{zz}^p(r, z) = -\int_{z(\phi)}^{z(\phi=0)} \Delta\rho g \phi(r, \zeta)\, \mathrm{d}\zeta \tag{3.6}$$

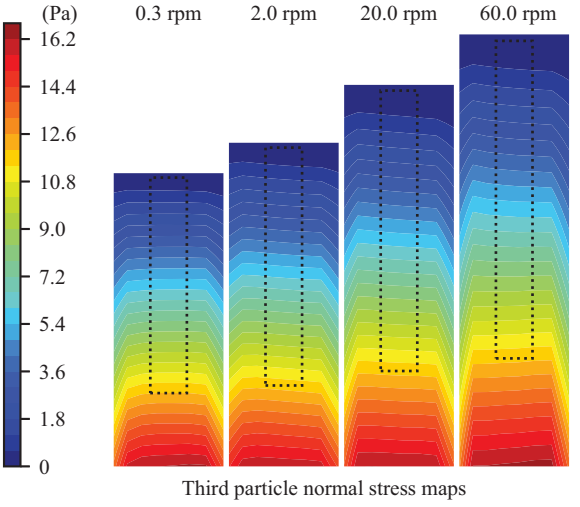

Figure 8. Maps of Σ^p_{33} for several angular velocities. The dashed rectangles indicate the areas that are used to measure Σ^p_{33} (figure 9) and to determine the variation of $\Sigma^p_{33}/\eta_0\dot{\gamma}$ with ϕ (figure 10). It is observed that, in these zones, Σ^p_{33} hardly varies along r.

with the boundary condition

$$\Sigma^p_{zz}\left(z(\phi = 0)\right) = \Sigma^p_{zz}(h_s) = 0. \tag{3.7}$$

Then, making the assumption that the flow is essentially one-dimensional, Σ^p_{zz} can be equated to Σ^p_{33}. Rigorously speaking, since the (z, θ) component of the shear rate is not exactly zero (see § 3.3.1), Σ^p_{22} also contributes to Σ^p_{zz}. This point is discussed in the supplementary material, where we show that the subsequent error is completely negligible compared with the scatter of the data.

Figure 8 displays the maps of Σ^p_{33} for four values of the angular velocity. It can be seen that, near the walls, in the regions where particle layering is observed, Σ^p_{33} is lower than in the bulk at a given z. Outside these zones, Σ^p_{33} hardly varies with r.

For each point $(r, z) \in [R_1 + (R_2 - R_1)/3 < r < R_2 - (R_2 - R_1)/3; z > h_s/4]$, the third particle normal stress, the local shear rate and the particle volume fraction are computed. Figure 9 shows the variation of $-\Sigma^p_{33}$ as a function of $\dot{\gamma}$ for several particle volume fractions. The particle volume fraction range is restricted to [0.3–0.5] because, in our experiment, for higher concentrations, the shear rate does not vary enough to obtain a reliable dependence between Σ^p_{33} and $\dot{\gamma}$ and, for lower concentrations, there are too few data (all contained in the very upper region of the resuspended layer) to extract the variation of Σ^p_{33} with $\dot{\gamma}$. From figure 9, it appears that, for a given value of ϕ, Σ^p_{33} varies with $\dot{\gamma}$ following a power law with an exponent close to 0.7. This result is in perfect agreement with the recent measurements of Saint-Michel *et al.* (2019). Shear thinning (i.e. a decrease of the viscosity with shear rate or shear stress) is an attribute of most non-Brownian concentrated suspensions (Acrivos *et al.* 1994; Vázquez-Quesada *et al.* 2016, 2017; Tanner *et al.* 2018; Lobry *et al.* 2019). Recently, it has been proposed that shear thinning comes from a non-Coulomb friction between particles (Chatté *et al.* 2018; Lobry *et al.* 2019). Thus the nonlinear scaling of Σ^p_{33} with $\dot{\gamma}$ is not surprising since particle normal stresses are expected to be scaled by the shear stress (Boyer *et al.* 2011; Lobry *et al.* 2019) leading to a nonlinear scaling law between Σ^p_{33} and $\dot{\gamma}$. More surprising is that there

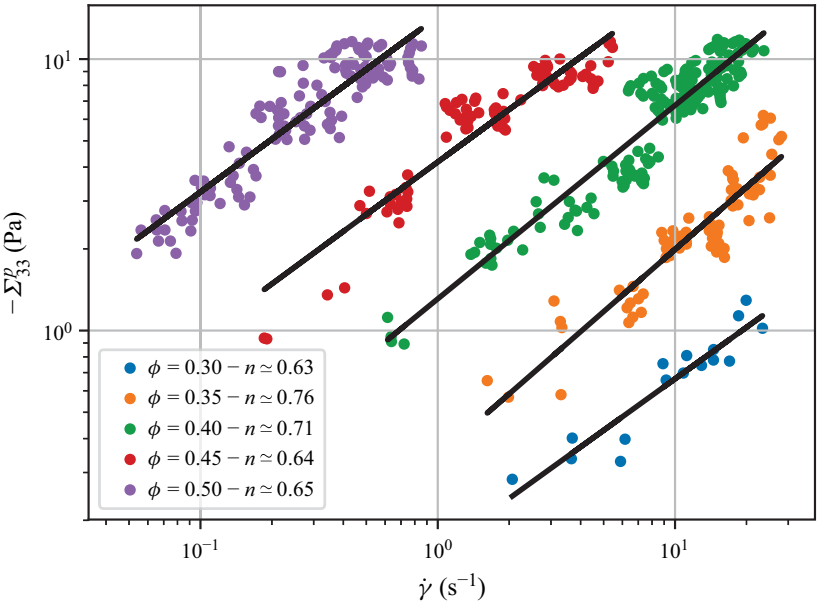

Figure 9. Variation of the third particle normal stress with shear rate for several particle volume fractions. Each set of data is fitted with a power law $\Sigma^p_{33} \propto \dot{\gamma}^n$.

is no clear variation of the exponent value with ϕ whereas shear thinning is known to be all the more pronounced where the particle volume fraction is large. This last observation would suggest that Σ^p_{33} might not vary linearly with shear stress. This could seem odd but can be justified by the fact that there is a fraction of Σ^p_{33} that is rate independent. Indeed, in a fully settled state, Σ^p_{33} is the result of the weight of particles borne by solid contact at the bottom wall. Thus, under shear, there will likely always be a fraction of Σ^p_{33} transmitted by this mechanism which is rate independent and may affect the apparent dependence on shear rate. To answer this question, it is probably necessary to perform combined measurements of both Σ^p_{33} and Σ_{12}, which is not possible in the present work since the vertical gradient of particle volume fraction prevents us from deducing Σ_{12} from the value of the torque applied to the rotor.

3.3.3. *Determination of* $\alpha_3 = \Sigma^p_{33}/\eta_0\dot{\gamma}$

The variation of $-\Sigma^p_{33}$ normalized by $\eta_0\dot{\gamma}$ as a function of ϕ is shown in figure 10 where we observe a reasonable collapse of the data onto a single curve for a wide range of ϕ between 0.15 and 0.55 with variation in $\Sigma^p_{33}/\eta_0\dot{\gamma}$ over more than five decades.

In figure 10(*a*), we restricted the data to particle volume fractions greater than 0.15 because, as shown in figure 5, below this value, the concentration profile is very sharp, which makes it difficult to measure the concentration. The data are somewhat scattered, especially for the largest values of ϕ. This finding may have different origins. First, it can stem from experimental issues because, as observed in figure 5, for the lowest angular velocity values (i.e. the larger particle volume fractions), the vertical concentration profile is nearly flat, which means that Σ^p_{33} given by the integral of $\phi(z)$ varies greatly with ϕ. Thus, even a small error in ϕ is likely to cause a large error in the computation of Σ^p_{33}. For lower concentrations, a better collapse can be obtained if, rather than $\Sigma^p_{33}/\dot{\gamma}$, $\Sigma^p_{33}/\dot{\gamma}^{0.7}$

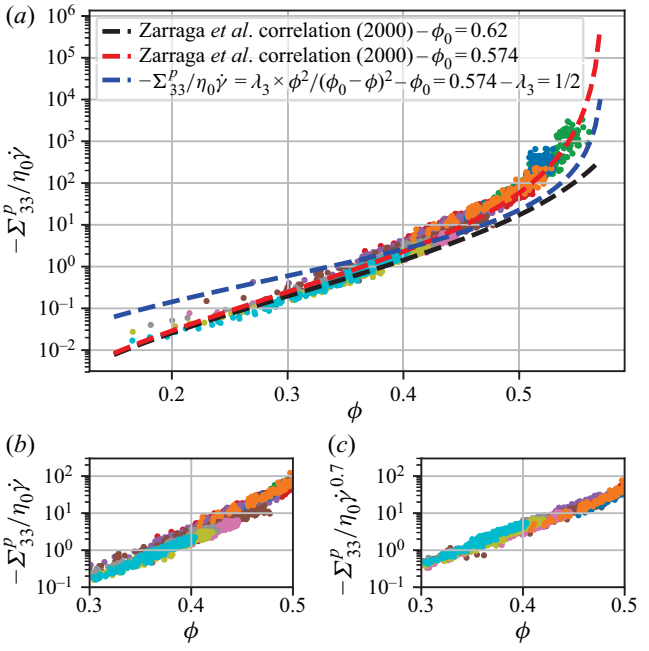

Figure 10. (*a*) Third particle normal stress normalized by the product of the fluid viscosity and the local shear rate versus the local particle volume fraction. The different colours correspond to different angular velocities of the rotor (see figure 7). The agreement with the correlation proposed by Zarraga *et al.* (2000) where $\phi_0 = 0.574$ is very good (red line). In contrast, it is not possible to represent the experimental results by the correlation obtained by Boyer *et al.* (2011) for Σ^p_{22} together with $\lambda_3 = 1/2$ (blue line). (*b*) Zoom of (*a*) for $\phi \in [0.3 - 0.5]$. (*c*) Variation of Σ^p_{33} divided by $\eta_0\dot{\gamma}^{0.7}$ versus ϕ. The collapse of the data is much better when the nonlinear power law is used.

is plotted against ϕ in the range $\phi \in [0.3 - 0.5]$ within which the power-law scaling has been obtained for Σ^p_{33} (see figure 10*b*,*c*). This is in agreement with the recent results of Saint-Michel *et al.* (2019).

The red and black lines in figure 10(*a*) represent the correlation proposed by Zarraga *et al.* (2000)

$$\Sigma^p_{33} = -\eta_0\dot{\gamma}\frac{\phi^3}{\left(1 - \dfrac{\phi}{\phi_0}\right)^3}. \tag{3.8}$$

The black curve is obtained with the original value of ϕ_0 proposed by Zarraga *et al.* (2000) ($\phi_0 = 0.62$), while the red curve has been obtained for $\phi_0 = 0.574$: the value of the particle volume fraction inside the settled layer that we measured. We observe a very good agreement between the experimental data and the correlation from Zarraga *et al.* (2000). Furthermore, Zarraga *et al.* (2000) established the correlation for a particle volume fraction ranging from 0.3 to 0.5, while our results show that this correlation can be expanded to a wider range of concentrations. The blue curve is obtained by using the correlation obtained by Boyer *et al.* (2011) for Σ^p_{22} (with $\phi_0 = 0.574$)

$$\Sigma^p_{22} = -\eta_0\dot{\gamma}\frac{\phi^2}{(\phi_0 - \phi)^2}, \tag{3.9}$$

and assuming that $\lambda_2 = \Sigma^p_{22}/\Sigma^p_{11} \approx 1$ and $\lambda_3 = \Sigma^p_{33}/\Sigma^p_{11} = 0.5$, as suggested by Morris & Boulay (1999).

The agreement between the blue curve and our data is not satisfactory. In our opinion, this discrepancy does not call into question the results obtained by Boyer *et al.* (2011) but rather the lack of variability in λ_3 with ϕ. This last result has already been noted by Gallier *et al.* (2014) and was previously suggested by Morris & Boulay (1999) themselves.

4. Concluding remarks

With the aim of studying viscous resuspension, we conducted local measurements of both the velocity and the particle volume fraction in a suspension of negatively buoyant non-Brownian spheres sheared in a cylindrical Couette flow. We observed a strong layering of the particles near the rotor and the stator. Outside these regions, the particle number density almost does not vary along r. If the suspension is considered as monodisperse (i.e. size segregation effects can be neglected), this result contrasts with the predictions of the SBM (Morris & Boulay 1999). Furthermore, the measured radial concentration profiles are inconsistent with the radial velocity profiles in the framework of local rheology of a (quasi-)Newtonian material. These discrepancies between predictions and experimental results on concentration and velocity profiles vanish for a neutrally buoyant suspension, as already noted by Blaj (2012), who showed that buoyant effects may be at the origin of shear localization even for particle volume fractions lower than the jamming fraction. This observation appears quite important and probably deserves further theoretical work to explore the role of buoyancy effects on suspension flows.

Besides this question, which remains open, we would like to underline the importance of measuring the local shear rate, at least in the context of the present study where, probably due to the use of a wide-gap Couette cell, the velocity profiles are far from what is expected.

The vertical concentration profiles are less startling. We reached almost the same results as Acrivos *et al.* (1993): the concentration slowly decreases from the bottom to the interface with the clear fluid and drops sharply to zero. The resuspension height is controlled by the Shields number (ratio between viscous and buoyancy forces) through a power-law relation with an exponent close to $1/3$, as already proposed by Acrivos *et al.* (1993). The vertical concentration profiles are used to deduce Σ^p_{33} by solving the Cauchy equation. We observed that Σ^p_{33} does not vary linearly with $\dot{\gamma}$ but follows a power law with an exponent close to 0.7. The value of the exponent hardly varies with particle concentration in the range $\phi \in [0.3 - 0.5]$. This result is in agreement with the recent findings of Saint-Michel *et al.* (2019) but raises questions. On the one hand, this nonlinear behaviour is anticipated since Σ^p_{33} is expected to be proportional to the shear stress, which itself varies less rapidly than linearly with shear rate (see for instance Tanner *et al.* (2018) or Lobry *et al.* (2019)). But, on the other hand, shear thinning is known to be all the more pronounced when the particle volume fraction is high. This should lead to exponents of the power law that decrease when ϕ increases, in contrast with what is observed.

Finally, concerning the variation of $\alpha_3 = \Sigma^p_{33}/\eta_0\dot{\gamma}$ with ϕ, we would like to make two comments. The first one is that our findings are in good agreement with the results of Zarraga *et al.* (2000), who deduced α_3 from the resuspension height measured by Acrivos *et al.* (1993). The second comment is that our results cannot be predicted by using the well-established correlation of Boyer *et al.* (2011) for Σ^p_{22} with the assumption that λ_3/λ_2 is constant, which should likely be revisited. It would probably be interesting to measure

accurately the three particle normal stresses and their variation with ϕ, in particular in order to refine the SBM that is a powerful framework for capturing migration.

Supplementary material. Supplementary material is available at https://doi.org/10.1017/jfm.2020.1074.

Acknowledgements. We thank L. Lobry, F. Peters and B. Saint-Michel for fruitful discussions, and D. Gilbert for the three-dimensional sketch of the experimental device.

Declaration of interests. The authors report no conflict of interest.

Author ORCIDs.
Elisabeth Lemaire https://orcid.org/0000-0001-8609-2783.

Appendix A. Vertical particle concentration profile in a neutrally buoyant suspension

Usually particle concentration profiles are determined from the measurement of the apparent area of particles crossed by the laser sheet. In most cases, this method is correct and suitable because the imaged zone is limited to a narrow cone of illumination. Here, the particle concentration has to be measured over a height of approximately 3.4 cm for the highest angular velocity. Thus, it is likely that the characteristics of the laser sheet (thickness, intensity) vary over this height, leading to bias in the particle concentration measurement. In order to identify these possible biases, we measured the vertical particle concentration profile in a neutrally buoyant suspension where $\phi(z)$ is expected not to vary. With this aim, we use the same experimental device as the one used to study resuspension except for the suspending liquid that has now the same density as the particles. We used a mixture of water (11.90 wt%), Triton X-100 (73.86 wt%) and zinc chloride (14.24 wt%) that matches both the density and the refractive index of PMMA particles (Souzy *et al.* 2015; Souzy, Pham & Metzger 2016). PMMA particles (Arkema BS572, $2a = 268 \pm 25$ μm) are added to this Newtonian mixture ($\eta_0 = 4.43$ Pa s) in order to obtain a suspension at $\phi = 0.52$. The suspension height in the Couette cell is set to 42 mm and, as in the case of the resuspension experiments, the suspension is presheared for a long period (10 h at $\Omega = 5$ r.p.m. which corresponds to an accumulated strain of approximately 10^4).

The steady vertical profile of the particle number density is shown in figure 11. As can be observed from this figure, $n(z)$ is almost constant except near the interface and, to a lesser extent, for $z > 29$ mm. As explained before, the decrease of n near the interface with mercury is due to light reflection on the metallic surface but this zone whose height is approximately 6 mm is never used to compute Σ_{33}^p. The decrease of n observed for $z > 29$ mm is probably due to a widening of the laser sheet which would stem from both the intrinsic geometry of the laser sheet and remaining light scattering, despite a good index matching. This bias introduces an error in the determination of Σ_{33}^p, which is computed from the integral of the vertical concentration profile from the interface between the suspension and the clear fluid. Nevertheless, resuspension height exceeds 29 mm only for the highest rotation speeds ($\Omega = 30$, 40 and 60 r.p.m.) and thus for the lowest particle volume fractions. For these low concentrations ($\phi \lesssim 0.3$), the ensuing error is anticipated to be smaller than the error measured with the 52 % suspension since the widening of the laser sheet and thus the subsequent bias is expected to decrease when the particle volume fraction decreases. Between $z = 7$ and 29 mm, n is definitely constant, contrarily to what is observed for the particle fraction deduced from the apparent area of particles crossed by the laser sheet (see figure 12) that continuously decreases when z increases.

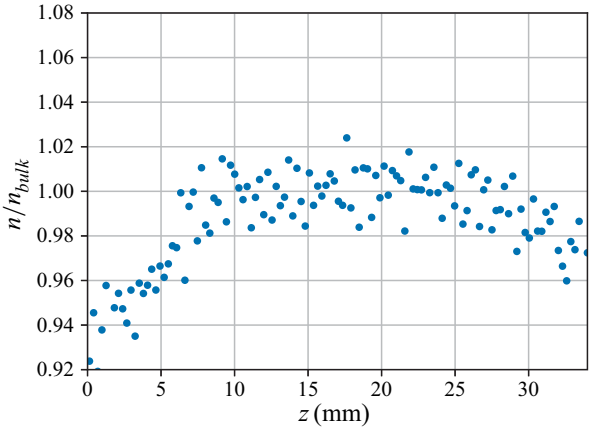

Figure 11. Variation of the particle number density with z normalized by the particle number density averaged over the central vertical quarter of the suspension. The profile is computed from 10 000 images with a vertical sampling $\delta z = 280\ \mu\text{m} \approx 2a$ and r-averaged over the central third of the gap.

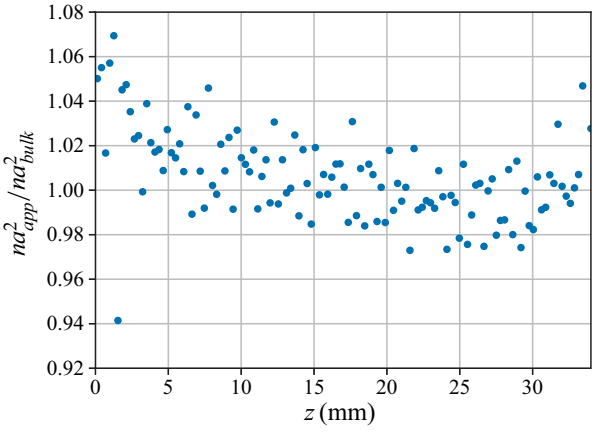

Figure 12. Vertical variation of the apparent solid area normalized by the solid area averaged over the central vertical quarter of the suspension, na^2_{bulk}. The profile is computed from 10 000 images with a vertical sampling $\delta z = 280\ \mu\text{m} \approx 2a$ and r-averaged over the central third of the gap.

For both methods, the bias is of the same order of magnitude (a few per cent) but the bias related to the first method affects the measurement of Σ^p_{33} only for the lowest concentrations ($\phi \lesssim 0.3$) while all values of Σ^p_{33} would be impaired by the detection bias attached to the second method. Based upon these findings, we conclude that, in our experimental configuration, it is more appropriate to deduce ϕ from n than from the particle area crossed by the laser sheet (proportional to $n\ a^2_{app}$), although using either method only marginally changes the results.

Appendix B. Radial particle concentration profile in a neutrally buoyant suspension

In this appendix, we want to examine the reasons why, in the resuspension experiments, we measured concentration and velocity profiles that are very different from what is

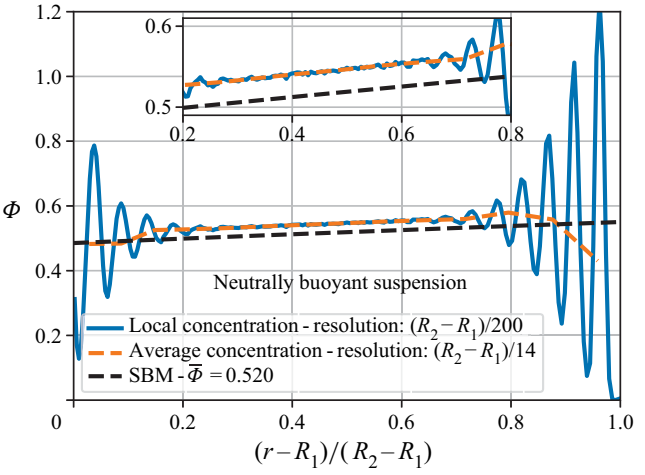

Figure 13. Radial concentration profiles measured for a neutrally buoyant suspension at $\phi = 0.52$. Blue line: spatial resolution has been fixed to one two-hundredths of the gap width $(R_2 - R_1)/200$, orange line: volume fraction average over $(R_2 - R_1)/14$. Dark dashed line: SBM prediction (Morris & Boulay 1999) computed for a bulk volume fraction of 0.52.

expected from the SBM (Morris & Boulay 1999) (see § 3.1). As a reminder, we identified two possible causes of this discrepancy: buoyancy or segregation effects. To discriminate between these two reasons, we measured the velocity and concentration profiles in a neutrally buoyant suspension. As stated in appendix A, the experimental device is exactly the same as the one used to study resuspension, the particles are the same, the experimental procedure (preshear, image processing…) is the same. Only the suspending liquid is changed. It now has the same density as the particles.

Figure 13 displays the radial concentration profile that has been measured. In blue, the spatial resolution has been fixed to one two-hundredths of the gap width and the orange line corresponds to the concentration profile averaged over one fourteenth of the gap width. As in the case of non-neutrally buoyant suspensions, a marked layering is observed but, outside these structured zones, the concentration varies along r, in contrast with what was observed for a non-neutrally buoyant suspension. The dark dashed line corresponds to the SBM predictions. We note that the slopes of the experimental and theoretical profiles are almost the same. The experimental profiles are somehow shifted toward higher volume fractions because, as indicated by the orange line, the concentration in the layered zones is smaller than the averaged volume fraction and thus higher outside these zones. Notwithstanding this difference, the agreement between the experimental and predicted profiles is good, suggesting that density mismatch between fluid and particles is responsible for the discrepancy observed between experimental and predicted concentration profiles displayed in figure 3. We also undertook the measurement of the velocity profile. Figure 14 shows the results obtained for $\Omega = 0.3$ r.p.m. (blue curve). For the sake of comparison, the Newtonian profiles without (solid line) and with (dashed line) slip conditions (3.3) have been plotted as well as the profiles computed from the predictions of the SBM ((3.1) and (3.2)), without (dotted line) and with (dash-dotted line) (3.3). The experimental velocity profile is very close to what was expected from the combination of wall slip conditions and SBM.

To conclude, the comparison of the velocity and concentration profiles obtained either for a neutrally or a non-neutrally buoyant suspension displays significant differences.

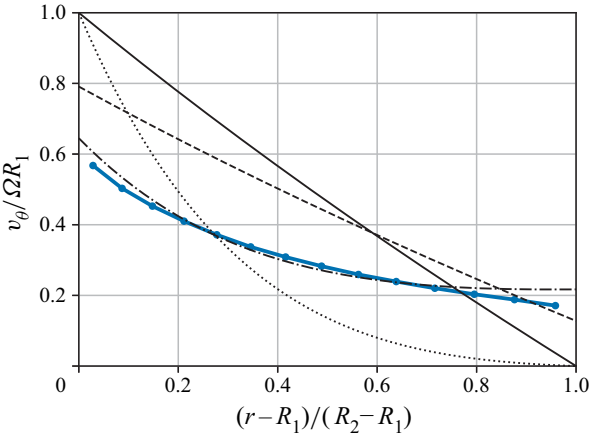

Figure 14. Normalized azimuthal velocity profiles. Blue line: measured for neutrally buoyant suspension at $\Omega = 0.3$ r.p.m. and $\phi = 0.52$. Are also shown the theoretical profiles. Solid line: Newtonian profile without wall slip, dashed line: Newtonian profile with wall slip evaluated from Jana *et al.* (1995) (3.3), dotted line: profile calculated according to (3.1) and (3.2) without wall slip, dash-dotted line: profile calculated according to (3.1) and (3.2) with wall slip (3.3).

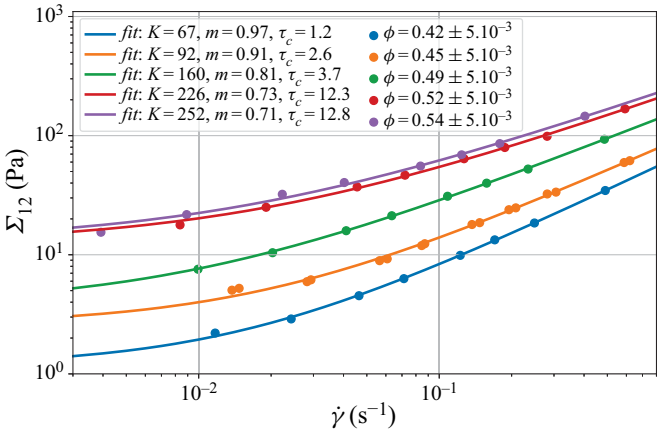

Figure 15. Variation of the local shear stress versus the local shear rate for different local particle concentrations. For each value of ϕ, the rheogram is fitted with a Herschel–Bulkley model: $\Sigma_{12} = \tau_c + K\dot{\gamma}^m$. The fitting parameters (in SI units) are given in the legend of the figure.

Furthermore, the SBM appears to reliably predict concentration profiles only if there is no density mismatch between the fluid and the particles. In this latter case, the SBM (Morris & Boulay 1999) computed with the correlation of Zarraga *et al.* (2000) (3.2) together with the slip boundary conditions proposed by Jana *et al.* (1995) (3.3) works well to describe the velocity profiles. However, in the case of a density mismatch between particles and fluid, the velocity profiles are much more heterogeneous.

Appendix C. Variation of the viscosity with particle volume fraction

In this appendix, we present local measurements of the viscosity as a function of particle volume fraction for the neutrally buoyant suspension. We were not able to measure

accurately the viscosity of the non-neutrally buoyant suspension since, due to the vertical particle volume fraction gradient, we do not know the vertical distribution of shear stress. On the other hand, performing macroscopic viscosity measurements, in a parallel plate geometry for example, seemed difficult, given the size of the particles. Indeed, in order to avoid wall effects (slip, structuring), it is necessary to work with gaps larger than approximately 15 times the particle size (Gallier *et al.* 2016), so, in our case, with a gap of more than 4 mm. For these reasons, we decided to measure the viscosity of the neutrally buoyant suspension but keeping in mind that it may not be exactly the same as that of the non-neutrally buoyant suspension.

The local measurements of viscosity are performed using the device described before and for suspensions with average particle volume fractions of between 0.4 and 0.52. For each of the experiments (i.e. each of the average volume fractions), the local volume fraction, $\phi(r, z)$ is measured after migration and the local shear rate $\dot{\gamma}(r, z)$ is computed from PIV measurements for different values of Ω. The values of ϕ and $\dot{\gamma}$ are then averaged over the height of the suspension so as to obtain the radial profiles $\phi(r)$ and $\dot{\gamma}(r)$. The shear stress is deduced from the torque applied to the rotor, Γ

$$\Sigma_{12} = \frac{\Gamma}{2\pi r^2 h}, \tag{C1}$$

where h is the height of the suspension.

For each of the average volume fractions, we select the radial position at which the volume fraction – averaged over h – is equal to a given value plus or minus 5×10^{-3}. We then report the variation of the shear stress as a function of the shear rate, measured at this radial position. Figure 15 shows this variation for five selected values of the particle volume fraction.

References

Abbott, J.R., Tetlow, N., Graham, A.L., Altobelli, S.A., Fukushima, E., Mondy, L.A. & Stephens, T.S. 1991 Experimental observations of particle migration in concentrated suspensions: Couette flow. *J. Rheol.* **35** (5), 773–795.

Acrivos, A., Fan, X. & Mauri, R. 1994 On the measurement of the relative viscosity of suspensions. *J. Rheol.* **38** (5), 1285–1296.

Acrivos, A., Mauri, R. & Fan, X. 1993 Shear-induced resuspension in a Couette device. *Intl J. Multiphase Flow* **19** (5), 797–802.

Ahuja, A. & Singh, A. 2009 Slip velocity of concentrated suspensions in Couette flow. *J. Rheol.* **53** (6), 1461–1485.

Blaj, O. 2012 Comment coule une pâte granulaire? Etudes des composantes primaire et secondaire et des fluctuations de l'écoulement. PhD theses, Université Sciences et Technologies – Bordeaux I.

Blaj, O., Merzeau, P., Snabre, P. & Pouligny, B. 2011 An automated single-particle tracker: application to characterization of non-azimuthal motion in Couette flows at low Reynolds number. *Exp. Fluids* **50** (6), 1559–1570.

Blanc, F., Lemaire, E., Meunier, A. & Peters, F. 2013 Microstructure in sheared non-Brownian concentrated suspensions. *J. Rheol.* **57** (1), 273–292.

Blanc, F., Peters, F. & Lemaire, E. 2011 Local transient rheological behavior of concentrated suspensions. *J. Rheol.* **55** (4), 835–854.

Boyer, F., Guazzelli, É. & Pouliquen, O. 2011 Unifying suspension and granular rheology. *Phys. Rev. Lett.* **107** (18), 188301.

Butler, J.E. & Bonnecaze, R.T. 1999 Imaging of particle shear migration with electrical impedance tomography. *Phys. Fluids* **11** (8), 1982–1994.

Chatté, G., Comtet, J., Niguès, A., Bocquet, L., Siria, A., Ducouret, G., Lequeux, F., Lenoir, N., Ovarlez, G. & Colin, A. 2018 Shear thinning in non-Brownian suspensions. *Soft Matt.* **14** (6), 879–893.

CHOW, A.W., IWAYIMA, J.H., SINTON, S.W. & LEIGHTON, D.T. 1995 Particle migration of non-Brownian, concentrated suspensions in a truncated cone-and-plate. In *Society of Rheology Meeting, Sacramento, CA*, vol. 103.

CHOW, A.W., SINTON, S.W., IWAMIYA, J.H. & STEPHENS, T.S. 1994 Shear-induced particle migration in Couette and parallel-plate viscometers: NMR imaging and stress measurements. *Phys. Fluids* **6** (8), 2561–2576.

COLBOURNE, A.A., BLYTHE, T.W., BARUA, R., LOVETT, S., MITCHELL, J., SEDERMAN, A.J. & GLADDEN, L.F. 2018 Validation of a low field Rheo-NMR instrument and application to shear-induced migration of suspended non-colloidal particles in Couette flow. *J. Magn. Reson.* **286**, 30–35.

DAI, S.-C., BERTEVAS, E., QI, F. & TANNER, R.I. 2013 Viscometric functions for noncolloidal sphere suspensions with Newtonian matrices. *J. Rheol.* **57** (2), 493–510.

DBOUK, T., LOBRY, L. & LEMAIRE, E. 2013 Normal stresses in concentrated non-Brownian suspensions. *J. Fluid Mech.* **715**, 239–272.

DEBOEUF, A., GAUTHIER, G., MARTIN, J., YURKOVETSKY, Y. & MORRIS, J.F. 2009 Particle pressure in a sheared suspension: a bridge from osmosis to granular dilatancy. *Phys. Rev. Lett.* **102** (10), 108301.

DEBOEUF, S., LENOIR, N., HAUTEMAYOU, D., BORNERT, M., BLANC, F. & OVARLEZ, G. 2018 Imaging non-Brownian particle suspensions with x-ray tomography: application to the microstructure of newtonian and viscoplastic suspensions. *J. Rheol.* **62** (2), 643–663.

GADALA-MARIA, F.A. 1979 The rheology of concentrated suspensions. PhD thesis, Stanford University.

GALLIER, S., LEMAIRE, E., LOBRY, L. & PETERS, F. 2016 Effect of confinement in wall-bounded non-colloidal suspensions. *J. Fluid Mech.* **799**, 100–127.

GALLIER, S., LEMAIRE, E., PETERS, F. & LOBRY, L. 2014 Rheology of sheared suspensions of rough frictional particles. *J. Fluid Mech.* **757**, 514–549.

GHOLAMI, M., RASHEDI, A., LENOIR, N., HAUTEMAYOU, D., OVARLEZ, G. & HORMOZI, S. 2018 Time-resolved 2D concentration maps in flowing suspensions using x-ray. *J. Rheol.* **62** (4), 955–974.

GRAHAM, A.L., ALTOBELLI, S.A., FUKUSHIMA, E., MONDY, L.A. & STEPHENS, T.S. 1991 Note: NMR imaging of shear-induced diffusion and structure in concentrated suspensions undergoing Couette flow. *J. Rheol.* **35** (1), 191–201.

GUAZZELLI, É. & POULIQUEN, O. 2018 Rheology of dense granular suspensions. *J. Fluid Mech.* **852**, P1.

HAMPTON, R.E., MAMMOLI, A.A., GRAHAM, A.L., TETLOW, N. & ALTOBELLI, S.A. 1997 Migration of particles undergoing pressure-driven flow in a circular conduit. *J. Rheol.* **41** (3), 621–640.

HUANG, N., OVARLEZ, G., BERTRAND, F., RODTS, S., COUSSOT, P. & BONN, D. 2005 Flow of wet granular materials. *Phys. Rev. Lett.* **94** (2), 028301.

JANA, S.C., KAPOOR, B. & ACRIVOS, A. 1995 Apparent wall slip velocity coefficients in concentrated suspensions of noncolloidal particles. *J. Rheol.* **39** (6), 1123–1132.

KOH, C.J., HOOKHAM, P. & LEAL, L.G. 1994 An experimental investigation of concentrated suspension flows in a rectangular channel. *J. Fluid Mech.* **266**, 1–32.

KORHONEN, M., MOHTASCHEMI, M., PUISTO, A., ILLA, X. & ALAVA, M.J. 2015 Apparent wall slip in non-Brownian hard-sphere suspensions. *Eur. Phys. J.* E **38** (5), 46.

LEIGHTON, D. & ACRIVOS, A. 1986 Viscous resuspension. *Chem. Engng Sci.* **41** (6), 1377–1384.

LHUILLIER, D. 2009 Migration of rigid particles in non-Brownian viscous suspensions. *Phys. Fluids* **21** (2), 023302.

LOBRY, L., LEMAIRE, E., BLANC, F., GALLIER, S. & PETERS, F. 2019 Shear thinning in non-Brownian suspensions explained by variable friction between particles. *J. Fluid Mech.* **860**, 682–710.

MANNEVILLE, S., BÉCU, L. & COLIN, A. 2004 High-frequency ultrasonic speckle velocimetry in sheared complex fluids. *Eur. Phys. J. Appl. Phys.* **28** (3), 361–373.

METZGER, B., RAHLI, O. & YIN, X. 2013 Heat transfer across sheared suspensions: role of the shear-induced diffusion. *J. Fluid Mech.* **724**, 527–552.

MEUNIER, P. & LEWEKE, T. 2003 Analysis and optimization of the error caused by high velocity gradients in PIV. *Exp. Fluids* **35**, 408–421.

MILLS, P. & SNABRE, P. 1995 Rheology and structure of concentrated suspensions of hard spheres. Shear induced particle migration. *J. Phys. II* **5** (10), 1597–1608.

MORRIS, J.F. & BRADY, J.F. 1998 Pressure-driven flow of a suspension: buoyancy effects. *Intl J. Multiphase Flow* **24** (1), 105–130.

MORRIS, J.F. & BOULAY, F. 1999 Curvilinear flows of noncolloidal suspensions: the role of normal stresses. *J. Rheol.* **43** (5), 1213–1237.

NOTT, P.R. & BRADY, J.F. 1994 Pressure-driven flow of suspensions: simulation and theory. *J. Fluid Mech.* **275**, 157–199.

NOTT, P.R., GUAZZELLI, E. & POULIQUEN, O. 2011 The suspension balance model revisited. *Phys. Fluids* **23** (4), 043304.

OVARLEZ, G., BERTRAND, F. & RODTS, S. 2006 Local determination of the constitutive law of a dense suspension of noncolloidal particles through magnetic resonance imaging. *J. Rheol.* **50** (3), 259–292.

OVARLEZ, G. & GUAZZELLI, E. 2013 Migration induite par cisaillement dans les suspensions. In *Congrès français de mécanique, AFM, Courbevoie, France*.

PHILLIPS, R.J., ARMSTRONG, R.C., BROWN, R.A., GRAHAM, A.L. & ABBOTT, J.R. 1992 A constitutive equation for concentrated suspensions that accounts for shear-induced particle migration. *Phys. Fluids* A **4** (1), 30–40.

RAMACHANDRAN, A. & LEIGHTON, D.T. 2008 The influence of secondary flows induced by normal stress differences on the shear-induced migration of particles in concentrated suspensions. *J. Fluid Mech.* **603**, 207–243.

SAINT-MICHEL, B., MANNEVILLE, S., MEEKER, S., OVARLEZ, G. & BODIGUEL, H. 2019 X-ray radiography of viscous resuspension. *Phys. Fluids* **31** (10), 103301.

SARABIAN, M., FIROUZNIA, M., METZGER, B. & HORMOZI, S. 2019 Fully developed and transient concentration profiles of particulate suspensions sheared in a cylindrical couette cell. *J. Fluid Mech.* **862**, 659–671.

SEGRE, G. & SILBERBERG, A. 1962 Behaviour of macroscopic rigid spheres in Poiseuille flow. Part 2. Experimental results and interpretation. *J. Fluid Mech.* **14** (1), 136–157.

SNOOK, B., BUTLER, J.E. & GUAZZELLI, É. 2016 Dynamics of shear-induced migration of spherical particles in oscillatory pipe flow. *J. Fluid Mech.* **786**, 128–153.

SOUZY, M., PHAM, P. & METZGER, B. 2016 Taylor's experiment in a periodically sheared particulate suspension. *Phys. Rev. Fluids* **1** (4), 042001.

SOUZY, M., YIN, X., VILLERMAUX, E., ABID, C. & METZGER, B. 2015 Super-diffusion in sheared suspensions. *Phys. Fluids* **27** (4), 041705.

SUZUKI, M., SHINMURA, T., IIMURA, K. & HIROTA, M. 2008 Study of the wall effect on particle packing structure using x-ray micro computed tomography. *Adv. Powder Technol.* **19** (2), 183–195.

TANNER, R.I., NESS, C., MAHMUD, A., DAI, S. & MOON, J. 2018 A bootstrap mechanism for non-colloidal suspension viscosity. *Rheol. Acta* **57** (10), 635–643.

VÁZQUEZ-QUESADA, A., MAHMUD, A., DAI, S., ELLERO, M. & TANNER, R.I. 2017 Investigating the causes of shear-thinning in non-colloidal suspensions: experiments and simulations. *J. Non-Newtonian Fluid Mech.* **248**, 1–7.

VÁZQUEZ-QUESADA, A., TANNER, R.I. & ELLERO, M. 2016 Shear thinning of noncolloidal suspensions. *Phys. Rev. Lett.* **117** (10), 108001.

VINCENT, L. & SOILLE, P. 1991 Watersheds in digital spaces: an efficient algorithm based on immersion simulations. *IEEE Trans. Pattern Anal. Mach. Intell.* (6), 583–598.

WESTERWEEL, J. 1997 Fundamentals of digital particle image velocimetry. *Meas. Sci. Technol.* **8** (12), 1379.

YEO, K. & MAXEY, M.R. 2010 Ordering transition of non-Brownian suspensions in confined steady shear flow. *Phys. Rev.* E **81** (5), 051502.

ZARRAGA, I.E., HILL, D.A. & LEIGHTON, D.T. JR. 2000 The characterization of the total stress of concentrated suspensions of noncolloidal spheres in Newtonian fluids. *J. Rheol.* **44** (2), 185–220.